Novel rotation scheme for dual-axis rotational inertial navigation system based on body diagonal rotation of inertial measurement unit

OPEN ACCESS
IOP Publishing
Measurement Science and Technology
Meas. Sci. Technol. **33** (2022) 095105 (11pp)
https://doi.org/10.1088/1361-6501/ac6e2c

Novel rotation scheme for dual-axis rotational inertial navigation system based on body diagonal rotation of inertial measurement unit

Qiushuo Wei, Feng Zha* and Lubin Chang

Department of Navigation, Naval University of Engineering, Wuhan, People's Republic of China

E-mail: zha_feng@126.com

Received 27 November 2021, revised 14 April 2022
Accepted for publication 9 May 2022
Published 15 June 2022

Abstract

Traditional rotational inertial navigation systems are based on rotation around one or two sensitive axes of inertial sensors. However, as the rotation and sensitive axes of inertial sensors lie along the same direction, it is difficult to modulate the relative error of the inertial sensor in the axial direction. This paper proposes a dual-axis rotation scheme based on the diagonal rotation of the inertial measurement unit (IMU) body. The scheme selects the body diagonal of the three orthogonal inertial sensors of the IMU as the horizontal rotation axis, and sets the vertical rotation axis orthogonal to this axis. As the rotation axis and the inertial sensor are oriented in different directions, at any moment of rotation, the errors of the inertial sensor in the three axial directions can all be modulated, especially the installation error. First, a mathematical model based on the diagonal rotation of the IMU body is established. On this basis, the coordinate transformation relationship and the error equations are derived, and the error propagation characteristics are obtained. Finally, the comprehensive error of the system is tested. Under the same error conditions, the system latitude error is reduced from 0.1089 nautical miles/72 h in the traditional scheme to 0.0368 nautical miles/72 h, and the longitude error is reduced from 0.3587 nautical miles/72 h to 0.1332 nautical miles/72 h. These results verify the effectiveness of the proposed scheme. This method of rotating around the body diagonal of the IMU also exhibits certain advantages when applied to other rotational inertial navigation schemes.

Keywords: rotational inertial navigation system, rotation scheme, error compensation

(Some figures may appear in colour only in the online journal)

* Author to whom any correspondence should be addressed.

1. Introduction

Inertial navigation systems (INSs) measure external information through inertial sensors, and then generate navigation information through integration processing. Thus, they have the characteristics of being autonomous and small, and achieve full space-time and all-weather navigation [1–6]. However, the errors of the inertial sensors will be integrated over time. At present, high-precision INSs mostly use rotation modulation technology to suppress the influence of inertial measurement unit (IMU) errors [7–15]. The constant drift and slow-varying errors of inertial sensors are the main factors affecting the accuracy of INSs. The rotational INS (RINS) uses the regular rotation of the IMU to compensate for these errors through different rotation sequences, so the design of the rotation scheme is the key to determining the improvement in system accuracy [16–23]. Common single- and dual-axial RINSs take one sensitive axis or two directional inertial sensors of the IMU as the rotation axis to produce different rotation schemes by changing the rotation speed, direction, and sequence of the rotation axis. Such schemes are simple and intuitive, have simple spatial relationships, and are easy to implement.

Since Levinson proposed the concept of rotational modulation in the 1980s [19], a number of rotational modulation schemes (RMSs) have been developed. They can mainly be divided into single-axis, two-axis, and three-axis RMSs. Among them, single- and dual-axis RMSs are more common, with three-axis RMSs less used because of the complex structure of the realization equipment and the influence of factors such as turntable errors. Single-axis rotational modulation can effectively suppress axial errors, except for those associated with the rotation axis, but the error in the direction of the rotation axis cannot be modulated. Sun *et al* [21] proposed an improved single-axis rotation scheme in which the angle between the rotation axis and the IMU sky axis is used to effectively modulate the error of the antenna component, thus improving the accuracy of the single-axis rotation system. Dual-axis rotation modulation is the most widely used scheme. This can be regarded as two single-axis alternate rotations, so the error in any axis can be compensated to a certain extent. Zhou *et al* [22] designed an eight-position rotation scheme based on the error compensation principle of the IMU, which optimizes the relationship between the installation error and rotation strategy. Xu *et al* [23] combined the motion constraint of the carrier with the rotation modulation to give a 32-position rotation scheme that enhances navigation accuracy. Zha *et al* [14] focused on the coupling effect between the scale factor error, installation error, and IMU rotation movement, and proposed a rotation scheme with comprehensive error suppression that reduces the accumulation of velocity errors in one cycle. Research on suitable rotation schemes is based on the premise that the rotation axis and the sensitive axis of the inertial sensor are in the same direction. As a result, when rotating around a certain axis, the relative error of the inertial sensor in the axial direction is difficult to modulate.

Using the principles of a single-axis rotation scheme, this paper proposes a dual-axis rotation scheme based on the diagonal rotation of the IMU body, following [14]. The solution no longer takes the sensitive axis of the inertial sensor as the rotation axis, but selects the body diagonals of the three orthogonal inertial sensors of the IMU as the horizontal rotation axis, and uses the vertical axis orthogonal to this axis as another rotation axis. By changing the rotation speed, direction, and sequence of horizontal and vertical rotating axes, it is possible to realize dual-axis rotation. Because the rotation axis and the inertial sensor are oriented in different directions, the device errors in the three directions perpendicular to the rotation axis can be modulated at any moment of rotation, which maximizes the accuracy of the system. A rigorous mathematical derivation and experimental simulation results prove that this scheme clearly suppresses the system installation errors.

2. Error model of dual-axis rotational INS

2.1. Definition of reference frames

Inertial frame (denoted as i): the origin of the inertial frame is at the center of the Earth. Its z-axis points in the direction of the north pole, the x-axis points toward the mean vernal equinox, and the y-axis completes the right-handed orthogonal frame. The inertial frame is non-rotating with respect to distant galaxies. The gyroscope and accelerometer outputs are relative to this frame.

Navigation frame (denoted as n): this frame is a local geodetic coordinate frame. Its origin is at the position of the vehicle and its x–y–z axes point east-north-up, respectively. The RINS calculation is performed in the navigation frame and, therefore, all vectors should be transformed into this frame before navigation calculations.

Body frame (denoted as b): this frame is defined as the orthogonal body-mounted IMU. Its x–y–z axes point right-forward-upward with respect to the vehicle, respectively. The relationship between the body frame and navigation frame encodes the attitude information of the ship.

Installation frame (denoted as m): the three gyroscopes and accelerometers are positioned vertical to each other, and the three groups of inertial elements give the x-axis, y-axis, and z-axis of the installation frame.

Rotation frame (denoted as p): at the initial moment of rotation modulation, the rotation frame coincides with the body frame. As the IMU rotates around the x-axis of the rotation frame, the x-axis of the rotation frame coincides with that of the body frame, and the y- and z-axes of the rotation frame rotate around the x-axis of the rotation angle speed. As the IMU rotates around the y-axis of the rotation frame, the y-axis of the rotation frame coincides with that of the body frame, and the x- and z-axes of the rotation frame rotate around the y-axis of the rotation angle speed. As the IMU rotates around the z-axis of the rotation frame, the z-axis of the rotation frame coincides with that of the body frame, and the x- and y-axes of the rotation frame rotate around the z-axis of the rotation angle speed. Dual-axis rotation modulation is generally achieved by rotating around the x- and z-axes.

2.2. Definition of system errors

Constant and random errors (denoted as ε and σ): the inertial sensor produces an output signal without an input signal. The input signal changes in a constant, random form.

Scale factor errors (denoted as δK): these errors are generated when the inertial sensor output voltage is converted to an angular velocity or acceleration. The scale factor error matrix is as follows:

$$\delta K = \begin{bmatrix} k_{11} & 0 & 0 \\ 0 & k_{22} & 0 \\ 0 & 0 & k_{33} \end{bmatrix}$$

where k_{11}, k_{22}, k_{33} denote the scale factor errors of the three gyroscopes or accelerometers.

Installation errors (denoted as δA): the angle between the sensitive axis of the inertial sensor and the ideal orthogonal installation. Let $k_{12}, k_{13}, k_{21}, k_{23}, k_{31}, k_{32}$ be the six installation error angles. The installation error matrix is as follows:

$$\delta A = \begin{bmatrix} 0 & k_{12} & k_{13} \\ k_{21} & 0 & k_{23} \\ k_{31} & k_{32} & 0 \end{bmatrix}.$$

2.3. Error propagation equations of RINS

In an INS, the attitude and velocity error equations based on the phi-angle-error definition are given by

$$\dot{\phi} = -\omega_{in}^{n} \times \phi + \delta\omega_{in}^{n} - C_b^n \delta\omega_{ib}^{b} \tag{1}$$

$$\begin{aligned} \delta\dot{v} = {} & f^n \times \phi + C_b^n \delta f^b - (2\omega_{ie}^{n} + \omega_{en}^{n}) \times \delta v \\ & - (2\delta\omega_{ie}^{n} + \delta\omega_{en}^{n}) \times v - \delta g \end{aligned} \tag{2}$$

where ϕ represents the misalignment angle of the 'mathematical platform'. v and δv denote the velocity and the velocity error, respectively, while ω and f denote the angular rate and the specific force, respectively. C_b^n denotes the attitude matrix. $\delta\omega_{ib}^{b}$ and δf^b denote the angular rate error and the specific force error.

The error propagation equation of the traditional RINS can be obtained from the error equation of the INS, as shown below:

$$\dot{\phi} = -\omega_{in}^{n} \times \phi + \delta\omega_{in}^{n} - C_b^n C_p^b \delta\omega_{ip}^{p} \tag{3}$$

$$\begin{aligned} \delta\dot{v} = {} & f^n \times \phi + C_b^n C_p^p \delta f^p - (2\omega_{ie}^{n} + \omega_{en}^{n}) \times \delta v \\ & - (2\delta\omega_{ie}^{n} + \delta\omega_{en}^{n}) \times v - \delta g \end{aligned} \tag{4}$$

where C_p^b denotes the coordinate transformation matrix from the rotational frame p to the body frame b. $\delta\omega_{ip}^{p}$ and δf^p denote the angular rate error and the specific force error measured in the frame p.

The third term in equation (3) is defined as the angular velocity error (denoted as E^n) in the navigation frame. The second term in equation (4) is the specific force error (denoted as Γ^n) in the navigation frame:

$$E^n = C_b^n C_p^b \delta\omega_{ip}^{p} = C_b^n C_p^b [(\delta K + \delta A)\omega_{ip}^{p} + \varepsilon^p + \sigma^p] \tag{5}$$

$$\Gamma^n = C_b^n C_p^b \delta f^p = C_b^n C_p^b [(\delta K + \delta A) f^p + \varepsilon^p + \sigma^p] \tag{6}$$

where ω_{ip}^{p} and f^p denote the angular rate and the specific force of the IMU relative to the inertial frame i.

3. Mathematical model of rotation scheme

3.1. Traditional rotation scheme modeling

The rotation scheme of [14] is based on the premise that the rotation axis and the sensitive axis of the inertial sensor are in the same direction. The specific rotation scheme can be expressed as follows:

(1) Rotate 180° about the positive Z-axis and rest for t_ss.
(2) Rotate 180° about the negative X-axis and rest for t_ss.
(3) Rotate 180° about the positive X-axis and rest for t_ss.
(4) Rotate 180° about the negative Z-axis and rest for t_ss.
(5) Rotate 180° about the negative X-axis and rest for t_ss.
(6) Rotate 180° about the positive Z-axis and rest for t_ss.
(7) Rotate 180° about the negative Z-axis and rest for t_ss.
(8) Rotate 180° about the positive X-axis and rest for t_ss.

Steps (9)–(16) of the rotation sequence are the same as (1)–(8), but with opposite rotation directions.

For the above-mentioned rotation scheme, the mutual relationship between the coordinate systems determines the rotation transformation matrix C_p^b and the rotation angular velocities ω^b and ω^p of the IMU under each rotation sequence in a rotation period. Expressions of the rotational angular velocities ω^b and ω^p with C_p^b and an IMU under the first four steps of the rotational sequence are listed in table 1.

3.2. Proposed rotation scheme

The scheme proposed in this paper is based on the traditional rotation scheme. The setting of the rotation axis is modified, the body diagonal of the three orthogonal inertial sensors of the IMU is selected as the horizontal rotation axis, and the vertical rotation axis is set to be orthogonal to this axis, as shown in figure 1.

The proposed scheme is based on the rotation scheme of [14], and changes the placement of the IMU on the dual-axis turntable. The body diagonal of the three orthogonal inertial sensors of the IMU gives the horizontal rotation axis, parallel to the inner ring axis of the turntable, and the direction orthogonal to this axis is the vertical rotation axis, parallel to the outer ring axis of the turntable. The angles between the horizontal rotation axis and the three sensitive axes of the IMU are equal, as shown in figure 2. The sequence of rotation is consistent with that in [14].

Table 1. Expressions of C_p^b and ω_{bp}^p in rotation sequence steps (1)–(4).

Rotation sequence	C_{pi}^b	ω_{bpi}^p	ω_{bpi}^p
1	$\begin{bmatrix} \cos\omega t & -\sin\omega t & 0 \\ \sin\omega t & \cos\omega t & 0 \\ 0 & 0 & 1 \end{bmatrix}$	$\begin{bmatrix} 0 \\ 0 \\ \omega \end{bmatrix}$	$\begin{bmatrix} 0 \\ 0 \\ \omega \end{bmatrix}$
2	$\begin{bmatrix} -1 & 0 & 0 \\ 0 & -\cos\omega t & \sin\omega t \\ 0 & \sin\omega t & \cos\omega t \end{bmatrix}$	$\begin{bmatrix} \omega \\ 0 \\ 0 \end{bmatrix}$	$\begin{bmatrix} -\omega \\ 0 \\ 0 \end{bmatrix}$
3	$\begin{bmatrix} -1 & 0 & 0 \\ 0 & \cos\omega t & \sin\omega t \\ 0 & \sin\omega t & -\cos\omega t \end{bmatrix}$	$\begin{bmatrix} -\omega \\ 0 \\ 0 \end{bmatrix}$	$\begin{bmatrix} \omega \\ 0 \\ 0 \end{bmatrix}$
4	$\begin{bmatrix} -\cos\omega t & -\sin\omega t & 0 \\ \sin\omega t & -\cos\omega t & 0 \\ 0 & 0 & 1 \end{bmatrix}$	$\begin{bmatrix} 0 \\ 0 \\ -\omega \end{bmatrix}$	$\begin{bmatrix} 0 \\ 0 \\ -\omega \end{bmatrix}$

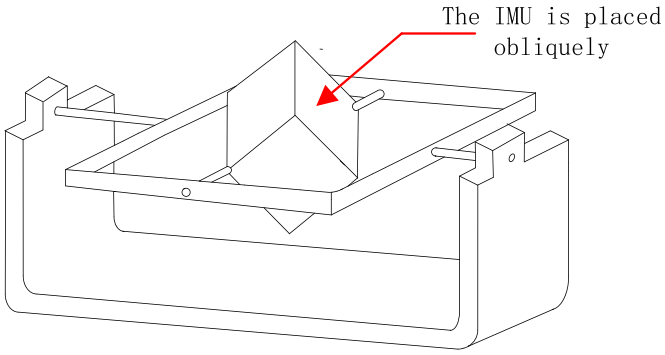

Figure 1. Tilt rotation modulation scheme.

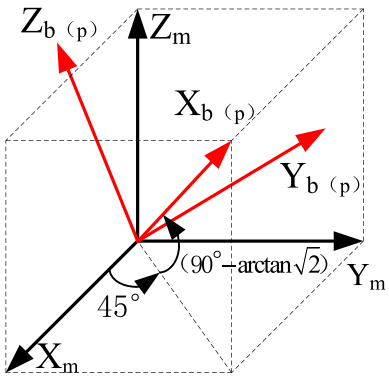

Figure 2. Relationship between installation frame and rotation frame.

The relationship between the installation frame and the rotation frame is now defined. As shown in figure 2, the rotation frame can be rotated around the Z-axis of the installation frame by 45° in the positive direction to give a rotation around the Y-axis of the installation frame in the negative direction $\left(90^\circ - \arctan\sqrt{2}\right)$. Thus, the coordinate transformation matrix C_m^p is obtained as follows:

$$C_m^p = \begin{bmatrix} \frac{\sqrt{3}}{3} & \frac{\sqrt{3}}{3} & -\frac{\sqrt{3}}{3} \\ -\frac{\sqrt{2}}{2} & \frac{\sqrt{2}}{2} & 0 \\ \frac{\sqrt{6}}{6} & \frac{\sqrt{6}}{6} & \frac{\sqrt{6}}{3} \end{bmatrix}.$$

Unlike the traditional rotation modulation axis, the body diagonal of the three orthogonal inertial sensors of the IMU is selected as the horizontal rotation axis, and the rotation axis orthogonal to this axis is the vertical rotation axis. The change in rotation axis modifies the error propagation equation, which requires the generation of a coordinate transformation matrix from the installation frame to the rotation frame. Thus, the new error propagation equation is expressed as

$$\dot{\phi} = -\omega_{in}^n \times \phi + \delta\omega_{in}^n - C_b^n C_p^b C_m^p \delta\omega_{im}^m \tag{7}$$

$$\begin{aligned} \delta\dot{v} = {} & f^n \times \phi + C_b^n C_p^b C_m^p \delta f^m - (2\omega_{ie}^n + \omega_{en}^n) \times \delta v \\ & - (2\delta\omega_{ie}^n + \delta\omega_{en}^n) \times v - \delta g \end{aligned} \tag{8}$$

where C_p^b denotes the coordinate transformation matrix from the rotation frame p to the body frame b. C_m^p denotes the coordinate transformation matrix from the installation frame m to the rotation frame p. $\delta\omega_{im}^m$ and δf^m denote the angular rate error and the specific force error measured in the installation frame.

The expansion formulas for the angular velocity error and the specific force error are as follows:

$$\begin{aligned} E^n &= C_b^n C_p^b C_m^p \delta\omega_{ip}^m \\ &= C_b^n C_p^b C_m^p [(\delta K + \delta A)\omega_{ip}^m + \varepsilon^m + \sigma^m] \end{aligned} \tag{9}$$

$$\begin{aligned} \Gamma^n &= C_b^n C_p^b C_m^p \delta f^m \\ &= C_b^n C_p^b C_m^p [(\delta K + \delta A) f^m + \varepsilon^m + \sigma^m]. \end{aligned} \tag{10}$$

It can be seen from these formulas that the RINS error is comparable to that of the strapdown inertial navigation system. There is a rotation matrix transfer; that is, the coordinate transformation matrix (C_p^b) from the rotation frame to the body frame, and an additional coordinate transformation matrix (C_m^p) from the installation frame to the rotation frame.

4. Analysis of system error characteristics

4.1. Attitude error analysis

According to equations (9) and (10), the error analysis for the accelerometer is similar to that for the gyroscope. The error analysis for the gyroscope is as follows. First, we discuss the attitude error caused by constant and random errors, scale factor errors, and installation errors.

Table 2. Attitude error caused by scale factor error and installation error in proposed rotation scheme.

Rotation sequence	$\phi_{\delta k}$	$\phi_{\delta A}$
1	$[\ 0 \quad 0 \quad \pi \quad k_1]^T$	$[\ 0 \quad 4\sqrt{2}k_2/3 \quad 5\pi k_2/3\ ]^T$
2	$[\ -\pi k_1 \quad 0 \quad \pi \quad k_1]^T$	$[\ 2\pi k_2/3 \quad 8\sqrt{2}k_2/3 \quad 5\pi k_2/3\ ]^T$
3	$[\ 0 \quad 0 \quad \pi \quad k_1]^T$	$[\ 0 \quad 4\sqrt{2}k_2/3 \quad 5\pi k_2/3\ ]^T$
4	$[\ 0 \quad 0 \quad 0\ ]^T$	$[\ 0 \quad 0 \quad 0\ ]^T$
5	$[\ -\pi k_1 \quad 0 \quad 0\ ]^T$	$[\ 2\pi k_2/3 \quad -4\sqrt{2}k_2/3 \quad 0\ ]^T$
6	$[\ -\pi k_1 \quad 0 \quad \pi k_1\ ]^T$	$[\ 2\pi k_2/3 \quad -8\sqrt{2}k_2/3 \quad 5\pi k_2/3\ ]^T$
7	$[\ -\pi k_1 \quad 0 \quad 0\ ]^T$	$[\ 2\pi k_2/3 \quad -4\sqrt{2}k_2/3 \quad 0\ ]^T$
8	$[\ 0 \quad 0 \quad 0\ ]^T$	$[\ 0 \quad 0 \quad 0\ ]^T$
9	$[\ 0 \quad 0 \quad -\pi k_1\ ]^T$	$[\ 0 \quad 4\sqrt{2}k_2/3 \quad -5\pi k_2/3\ ]^T$
10	$[\ \pi k_1 \quad 0 \quad -\pi k_1\ ]^T$	$[\ -2\pi k_2/3 \quad 8\sqrt{2}k_2/3 \quad -5\pi k_2/3\ ]^T$
11	$[\ 0 \quad 0 \quad -\pi k_1\ ]^T$	$[\ 0 \quad 4\sqrt{2}k_2/3 \quad -5\pi k_2/3\ ]^T$
12	$[\ 0 \quad 0 \quad 0\ ]^T$	$[\ 0 \quad 0 \quad 0\ ]^T$
13	$[\ \pi k_1 \quad 0 \quad 0\ ]^T$	$[\ -2\pi k_2/3 \quad -4\sqrt{2}k_2/3 \quad 0\ ]^T$
14	$[\ \pi k_1 \quad 0 \quad -\pi k_1\ ]^T$	$[\ -2\pi k_2/3 \quad -8\sqrt{2}k_2/3 \quad -5\pi k_2/3\ ]^T$
15	$[\ \pi k_1 \quad 0 \quad 0\ ]^T$	$[\ -2\pi k_2/3 \quad -4\sqrt{2}k_2/3 \quad 0\ ]^T$
16	$[\ 0 \quad 0 \quad 0\ ]^T$	$[\ 0 \quad 0 \quad 0\ ]^T$

4.1.1. Analysis of attitude error caused by constant error and random error. Rotating the IMU once around the rotation Z-axis and once around the rotation X-axis as an example, the constant error in equation (9) is integrated as follows:

$$\begin{aligned}\phi &= \int_0^{2\pi/\omega} \mathrm{E}_\varepsilon^n \mathrm{d}t = \int_0^{2\pi/\omega} C_b^n C_p^b C_m^p \varepsilon^m \mathrm{d}t \\ &= \int_0^{2\pi/\omega} C_m^p \begin{bmatrix} \varepsilon_x^m \cos\omega t - \varepsilon_y^m \sin\omega t \\ \varepsilon_x^m \sin\omega t + \varepsilon_y^m \cos\omega t \\ \varepsilon_z^m \end{bmatrix} \mathrm{d}t = \begin{bmatrix} -\varepsilon_z^m \frac{2\sqrt{3}\pi}{3\omega} \\ 0 \\ \varepsilon_z^m \frac{2\sqrt{6}\pi}{3\omega} \end{bmatrix}\end{aligned} \tag{11}$$

$$\begin{aligned}\phi &= \int_0^{2\pi/\omega} \mathrm{E}_\varepsilon^n \mathrm{d}t = \int_0^{2\pi/\omega} C_b^n C_p^b C_m^p \varepsilon^m \mathrm{d}t \\ &= \int_0^{2\pi/\omega} C_m^p \begin{bmatrix} \varepsilon_x^m \\ \varepsilon_y^m \cos\omega t - \varepsilon_z^m \sin\omega t \\ \varepsilon_y^m \sin\omega t + \varepsilon_z^m \cos\omega t \end{bmatrix} \mathrm{d}t = \begin{bmatrix} \varepsilon_x^m \frac{2\sqrt{3}\pi}{3\omega} \\ -\varepsilon_x^m \frac{\sqrt{2}\pi}{\omega} \\ \varepsilon_x^m \frac{\sqrt{6}\pi}{3\omega} \end{bmatrix}.\end{aligned} \tag{12}$$

Equations (11) and (12) indicate that, although different from the traditional rotation scheme, errors other than those of the rotation axis can be modulated to zero. However, the posture error after modulation is constant, so after rotating around the X- and Z-axes alternately, the attitude errors caused by the constant errors of the three orthogonal gyroscopes can be modulated into a zero-average periodic form.

Attitude errors caused by random errors remain in random form after multiplying, integrating, and summing the sine and cosine functions. Therefore, rotation modulation cannot change the randomness of attitude errors caused by random errors.

4.1.2. Analysis of attitude error caused by scale factor error. Integrating and accumulating the part containing the scale factor error in equation (9) gives the attitude error variation range caused by the scale factor error after each rotation. Equation (13) gives the attitude error caused by the scale factor error in one rotation period (that is, after 16 rotations):

$$\phi_{\delta K} = \int_0^{\pi/\omega} \sum_{i=0}^{16} E_{\delta K}^n \mathrm{d}t = \int_0^{\pi/\omega} \sum_{x=0}^{16} (C_b^n C_{px}^b C_{mx}^{px} \delta K \omega_x^m) \mathrm{d}t. \tag{13}$$

4.1.3. Analysis of attitude error caused by installation error. Integrating and accumulating the part containing the installation error in equation (9) gives the attitude error variation range caused by the installation error after each rotation. Equation (14) shows the attitude error caused by the installation error in a rotation period:

$$\phi_\delta\ \mathrm{A} = \int_0^{\pi/\omega} \sum_{i=0}^{16} E_\delta \mathrm{A}^n \mathrm{d}t = \int_0^{\pi/\omega} \sum_{x=0}^{16} (C_b^n C_{px}^b C_{mx}^{px} \delta\ \mathrm{A} \omega_x^m) \mathrm{d}t. \tag{14}$$

Incorporating the above-mentioned mathematical expressions related to the proposed rotation scheme into equations (13) and (14), the attitude error caused by the scale factor error and the installation error can be obtained.

As in [14], we assume that the scale factor errors of the three groups of inertial sensors are the same, and the installation errors of each axis are equal. Suppose that $k_{11} = k_{22} = k_{33} = k_1$, $k_{12} = k_{13} = k_{21} = k_{23} = k_{31} = k_{32} = k_2$. The attitude errors after each rotation sequence are as listed in table 2.

The attitude error caused by the scale factor error and the installation error in [14] can be written in a similar form as in table 2, allowing the amplitude changes to be compared.

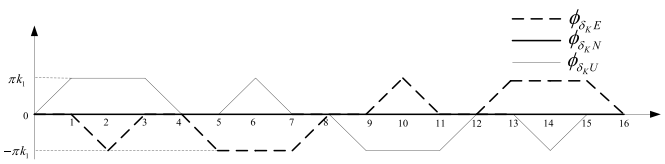

Figure 3. Comparison of attitude error caused by scale factor error between two rotation schemes.

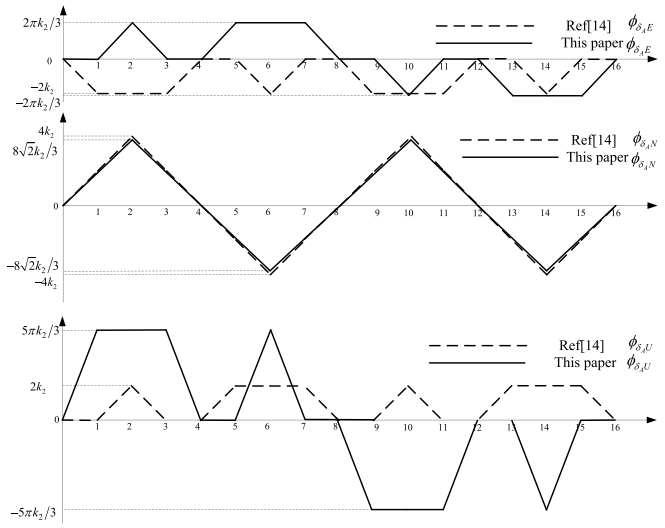

Figure 4. Comparison of attitude error caused by installation error between two rotation schemes.

Figures 3 and 4 compare the changes in the attitude error amplitude caused by the scale factor error and installation error of the two schemes.

As shown in figure 3, the attitude error amplitude changes caused by the scale factor errors of the two schemes are the same, i.e. always zero on the north axis, and the attitude errors on the east axis and the up axis are modulated into a periodic form with a mean value of zero. Thus, the scale factor error is not integrated and will not cause the velocity error to accumulate.

As can be seen from figure 4, the attitude error caused by the installation error under the two schemes is modulated into different forms. In the scheme of [14], the north component of the attitude error is modulated into a periodic form with a zero mean, while the mean value of the east and up error components of the attitude is not zero. In the proposed scheme, the attitude error components along the north, east, and up axes are all modulated into a zero-average periodic form. In the INS, the attitude error further affects the system velocity error, so the difference in modulation characteristics between the two schemes will cause different error modulation effects. These will be analyzed in detail in the next section. In addition, the maximum amplitude of the north component of the attitude error in the proposed scheme is smaller than in the scheme of [14], decreasing from $4k_2$ to $8\sqrt{2}k_2\big/3$. Therefore, the main feature of the proposed scheme is that it has obvious advantages in restraining the installation errors.

4.2. Velocity error analysis

It can be seen from equation (8) that when the system has an attitude error of ϕ, this will be coupled with the carrier force to produce a velocity error increment of $\delta\dot{v}$. The velocity error increment can be integrated to obtain the velocity error caused by the attitude error:

$$\delta v = \int (f^n \times \phi)\mathrm{d}t \tag{15}$$

$$f^n = \begin{bmatrix} 0 & 0 & g \end{bmatrix}^T. \tag{16}$$

Based on the static carrier present mentioned above, f^n can be expressed as in equation (16), where g is the local gravitational acceleration. Therefore, the velocity errors along the north and east axes can be written as follows:

$$\delta v_E = \int (-\phi_N g)\mathrm{d}t \tag{17}$$

$$\delta v_N = \int (\phi_E g)\mathrm{d}t. \tag{18}$$

Equation (13) can be added to equation (14) to find the attitude error caused by the scale factor error and the installation error. Substituting these quantities into equations (17) and (18), the velocity errors in the north and east axes can be obtained. To determine the magnitude of the error range of the velocity errors of the two schemes along the north axis, it is assumed that the scale factor errors of the three groups of inertial sensors are the same, and the installation errors of each axis are equal. Suppose that $t_r = \pi/\omega$, $k_{11} = k_{22} = k_{33} = k_1$, $k_{12} = k_{13} = k_{21} = k_{23} = k_{31} = k_{32} = k_2$. The simplified north-axis velocity error after each step is listed in table 3.

It can be concluded from table 3 that the scheme of [14] (average amplitude: $-3.25k_2gt_r$) and the proposed scheme (average amplitude: $(-8\sqrt{2}k_2\big/3)gt_r$) have very similar average amplitudes of the east-axis velocity error. The two schemes have the same change in amplitude of the north-axis velocity error accumulation caused by the scale factor error, which reflects the modulation effect of the proposed scheme in suppressing the accumulation of system velocity errors caused by the installation error. For example, in [14], the cumulative average amplitude of the north-axis velocity error caused by the installation error is $-10k_2gt_r$, and the average amplitude of the proposed scheme is $4k_2\big/3gt_r$. In terms of amplitude, the north-axis velocity error of the proposed scheme is relatively small.

To illustrate that the magnitude of the north-axis velocity error in the proposed scheme is small, the cumulative magnitude of this error caused by the installation error listed in table 3 is shown in figure 5. This figure illustrates that, under the proposed tilt scheme, the rotation modulation scheme of [14] can reduce the accumulation of the north-axis velocity error caused by installation error, so that the position error can be fully modulated.

Table 3. Velocity error caused by scale factor error and installation error in proposed rotation scheme.

Rotation sequence	δv_E	δv_N
1	$(-4\sqrt{2}k_2/3)gt_r$	0
2	$(-4\sqrt{2}k_2)gt_r$	$(2k_2/3-\pi k_1)gt_r$
3	$(-16\sqrt{2}k_2/3)gt_r$	$(2k_2/3-\pi k_1)gt_r$
4	$(-16\sqrt{2}k_2/3)gt_r$	$(2k_2/3-\pi k_1)gt_r$
5	$(-4\sqrt{2}k_2)gt_r$	$(4k_2/3-2\pi k_1)gt_r$
6	$(-4\sqrt{2}k_2/3)gt_r$	$(6k_2/3-3\pi k_1)gt_r$
7	0	$(8k_2/3-4\pi k_1)gt_r$
8	0	$(8k_2/3-4\pi k_1)gt_r$
9	$(-4\sqrt{2}k_2/3)gt_r$	$(8k_2/3-4\pi k_1)gt_r$
10	$(-4\sqrt{2}k_2)gt_r$	$(6k_2/3-3\pi k_1)gt_r$
11	$(-16\sqrt{2}k_2/3)gt_r$	$(6k_2/3-3\pi k_1)gt_r$
12	$(-16\sqrt{2}k_2/3)gt_r$	$(6k_2/3-3\pi k_1)gt_r$
13	$(-4\sqrt{2}k_2)gt_r$	$(4k_2/3-2\pi k_1)gt_r$
14	$(-4\sqrt{2}k_2/3)gt_r$	$(2k_2/3-\pi k_1)gt_r$
15	0	0
16	0	0
Mean	$(-8\sqrt{2}k_2/3)gt_r$	$(4k_2/3-2\pi k_1)gt_r$

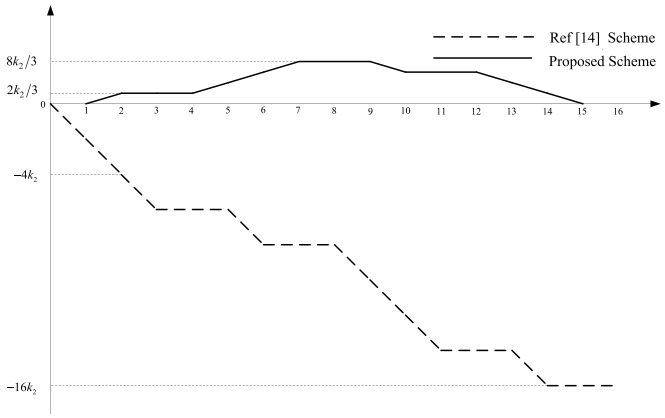

Figure 5. Comparison of error amplitude of north-axis velocity.

Ignoring the influence of the height factor, the position error equation is

$$\delta\dot{L} = \frac{\delta v_N}{R_M} \tag{19}$$

$$\delta\dot{\lambda} = \frac{\delta v_E}{R_N \cos L} + \delta L \frac{v_E}{R_N} \tan L \sec L \tag{20}$$

where R_M is the radius of curvature of the meridian circle and R_N is the radius of curvature of the unitary circle.

Equations (19) and (20) indicate that a decrease in the velocity errors along the north axis leads to a decrease in the latitude error and the longitude error.

Table 4. Experimental conditions.

Parameter	Value
Latitude	30.58°
Longitude	114.23°
Roll angle	$3^\circ sin(2\pi t/7)$
Pitch angle	$5^\circ sin(\pi t/6)$
Heading	$0.5^\circ sin(\pi t/4)$
Turntable speed	$6^\circ/s$
Rotation and rest time	30 s
Gyro zero bias	$0.001^\circ/h$
Gyro random error	$0.0003^\circ/\sqrt{h}$
Gyro scale factor error	5 ppm
Gyro installation error	$5''$
Accelerometer zero bias	10 μg
Accelerometer random error	1 μg
Accelerometer scale factor error	10 ppm
Accelerometer installation error	$10''$

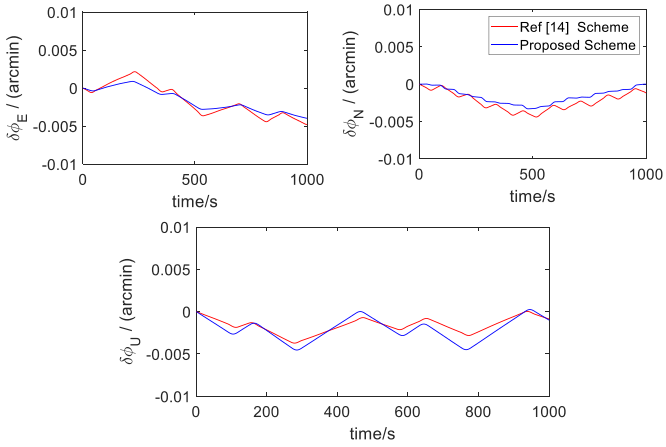

Figure 6. Comparison of attitude errors caused by constant errors.

5. Simulations and analysis

To verify the correctness of the mathematical derivation and analysis of the proposed tilt scheme and the effect of its actual application, simulation experiments were carried out. The specific simulation parameter settings are listed in table 4.

5.1. Simulation of constant error, scale factor error, and installation error

To verify the analysis of the attitude error caused by the constant error, scale factor error, and installation error, three simulations were conducted. Each simulation considered either a constant error, scale factor error, or installation error.

The results of the simulation, including the constant value error listed in table 4, are shown in figure 6. This figure compares the attitude error caused by the constant error in one cycle (960 s) between the rotation scheme in [14] and the proposed rotation scheme. The trends in the attitude error amplitude caused by the constant value error are similar, and the attitude errors are close to zero. This verifies our mathematical derivation of the effects of a constant error.

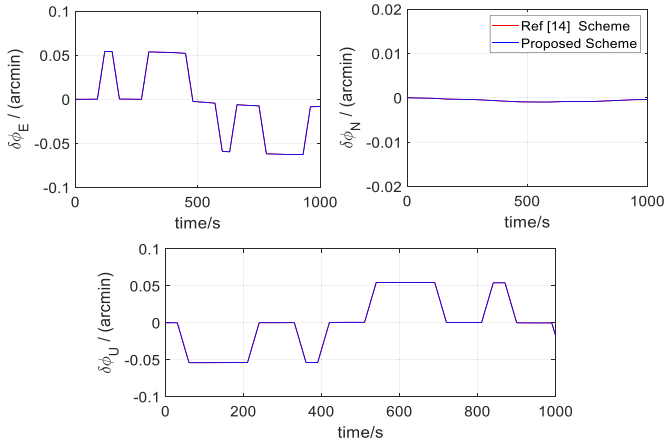

Figure 7. Comparison of attitude errors caused by scale factor errors.

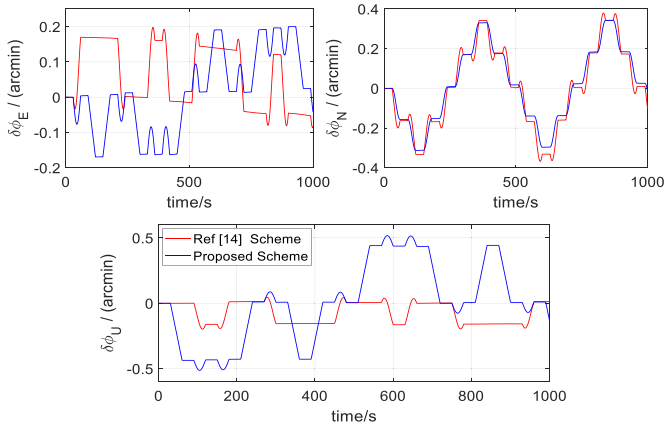

Figure 8. Comparison of attitude errors caused by installation errors.

The simulation results considering the scale factor error listed in table 4 are shown in figure 7. The attitude error caused by the scale factor error in the rotation scheme of [14] is compared with that resulting from the proposed rotation scheme in one cycle (960 s). Combining these results with figure 3, we find that the changes in the attitude error amplitude caused by the scale factor error are the same for the two schemes. Thus, as shown in figure 7, the data curve of the proposed rotation scheme covers the scheme of [14].

The simulation results for the installation error listed in table 4 are shown in figure 8, which compares the attitude errors of the two rotation schemes. The proposed rotation scheme not only modulates the attitude error of the north axis into a periodic form with a mean of zero, but also modulates the east-axis and the up-axis attitude errors into the form of a zero-average period. This result verifies the correctness of the mathematical derivation in table 3 and figure 3.

To verify the correctness of the mathematical derivation of the velocity error, an experimental simulation was conducted using only the installation error. The experimental results are shown in figure 9. Compared with the scheme of [14], the

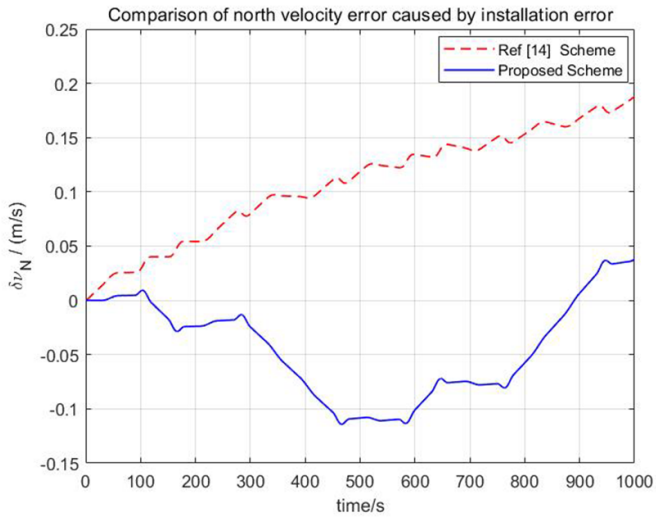

Figure 9. Comparison of north velocity errors caused by installation errors.

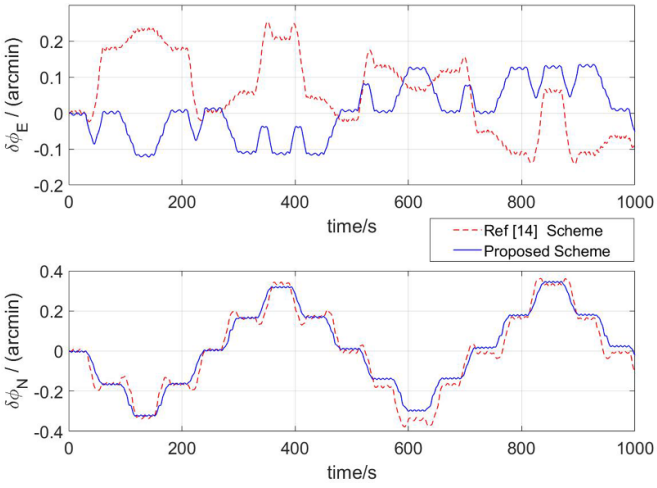

Figure 10. Comparison of x- and y-axis attitude errors in one cycle.

velocity error of the proposed scheme is significantly reduced, and the change trend is consistent with that in figure 5.

5.2. Comprehensive error simulations

To test the effectiveness of the proposed scheme in practical applications, the main error sources were identified, and comprehensive error simulations were performed. The parameter settings are listed in table 4. The attitude error and velocity error caused by the combined error in one cycle (960 s) are shown in figures 10 and 11.

The attitude error, velocity error, and position error caused by the combined error during a long sailing time (72 h) are shown in figures 12 and 13.

As shown in figure 10, compared with the scheme of [14], the proposed method modulates the x-axis attitude error into a zero-average periodic form. The scheme described in

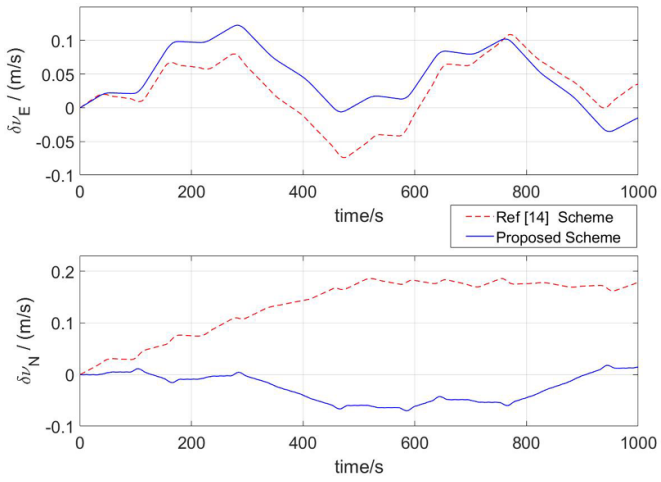

Figure 11. Comparison of east- and north-axis velocity errors in one cycle.

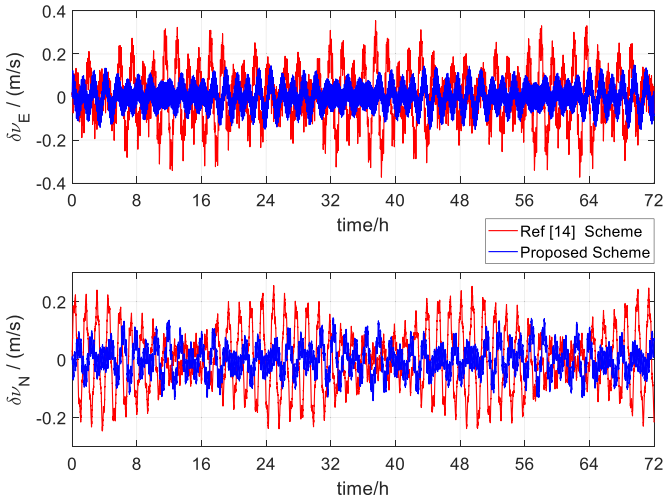

Figure 13. Comparison of east- and north-axis velocity errors over three days.

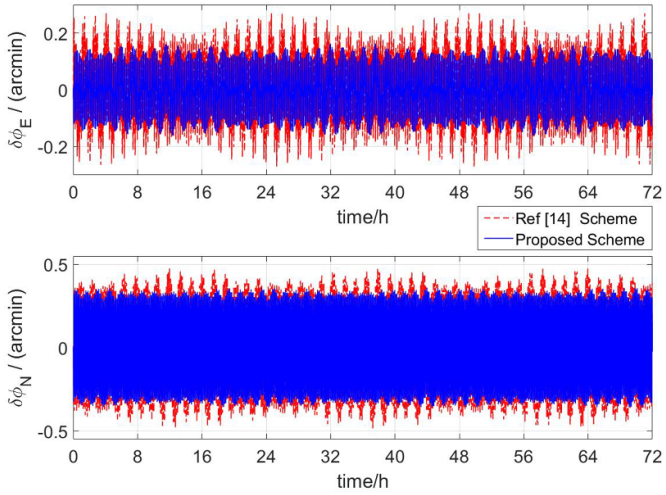

Figure 12. Comparison of *x*- and *y*-axis attitude errors over three days.

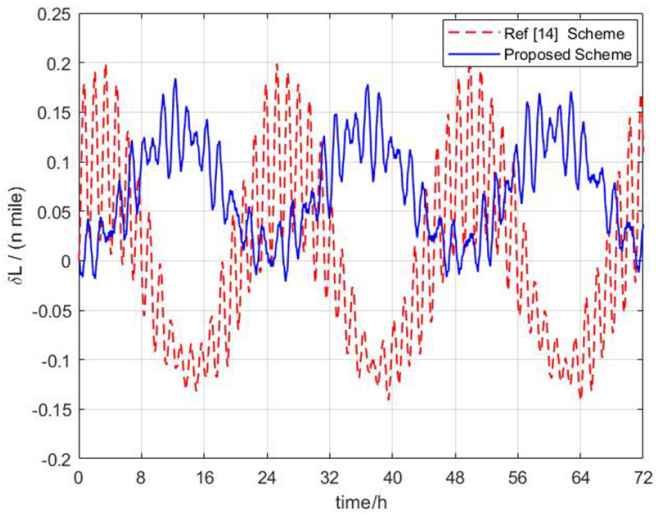

Figure 14. Comparison of latitude errors over three days.

this paper mainly reflects the modulation effect of the system *x*-axis attitude error on the modulation of the installation error. As a result, the accumulation of velocity errors along the north-axis is correspondingly reduced. The *y*-axis attitude error range suppression ability of the proposed scheme is similar to that of [14], so the velocity errors that accumulate along the east axis are similar. Therefore, figure 11 fully proves the correctness of the theoretical derivation.

According to equations (19) and (20) and the above analysis, compared with the scheme of [14], the rotation modulation of the proposed scheme reduces the velocity errors along the north axis of the system, and the position error is reduced accordingly, as shown in figures 14 and 15. The latitude error of the proposed scheme decreases from 0.1089 nautical miles/72 h [14] to 0.0368 nautical miles/72 h, and the longitude error decreases from 0.3587 nautical miles/72 h [14] to 0.1332 nautical miles/72 h. This shows that the longitude error increases slowly with the increasing sailing time.

To verify the applicability of the body diagonal rotation scheme proposed in this paper, in addition to comparing it with the scheme of [14], the eight-position rotation scheme in [9] and the 16-position rotation scheme in [24] are also compared. The experimental conditions are as listed in table 4. The position errors under the proposed scheme are compared with those under the schemes described in [9] and [24] in figures 16 and 17, respectively.

As shown in figures 16 and 17, when the rotation schemes in [9] and [24] are applied to the diagonal rotation of the IMU around the body, a certain accuracy improvement can be achieved. Therefore, the rotational modulation technique based on the diagonal of the IMU body has clear research value.

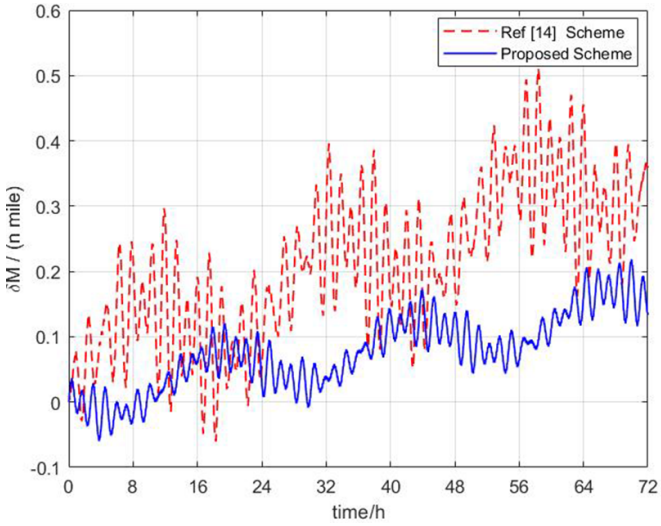

Figure 15. Comparison of longitude errors over three days.

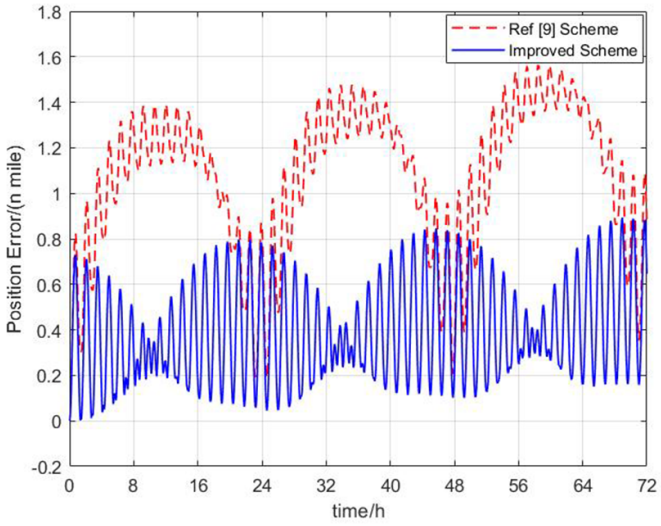

Figure 16. Comparison of position error of the scheme in [9] and the improved scheme.

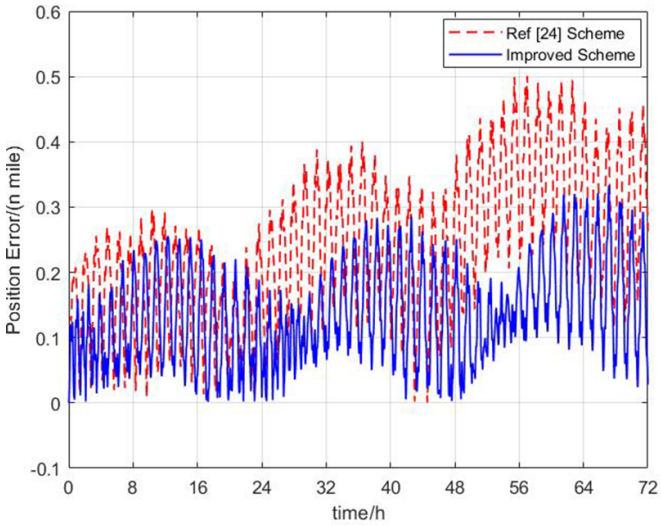

Figure 17. Comparison of position error of the scheme in [24] and the improved scheme.

6. Conclusion

The error compensation of RINSs depends on the design of the rotation scheme. Unlike the traditional rotation scheme, this article describes a method in which the IMU is rotated based on the diagonal of the body. This approach does not introduce new errors and reduces the various existing errors, especially through the modulation effect on the installation error. Simulations show that the proposed method based on the body diagonal rotation reduces the latitude error of the scheme in [14] from 0.1089 nautical miles/72 h to 0.0368 nautical miles/72 h and the longitude error from 0.3587 nautical miles/72 h to 0.1332 nautical miles/72 h. The proposed scheme also slows the increase in longitude error with the increasing voyage time. Applying the method of rotating around the IMU to other schemes also produces certain advantages.

Future work will investigate the application of the improved scheme to real-world scenarios. This will involve installing the IMU on a certain datum plane, and ensuring that the three sets of inertial devices are orthogonal through the orthogonal datum plane of the cube. The diagonal vertex of the cube will then be set as the axis, allowing the rotation axis to be constructed. As this method of construction will inevitably introduce errors, the constructed IMU will be calibrated on a laboratory turntable, with error items such as the non-orthogonal error and shaft installation error calibrated by standard angular velocity excitation. The current turntable calibration accuracy can reach the arc-second level.

Data availability statement

No new data were created or analyzed in this study.

Acknowledgments

This work was supported by the National Natural Science Foundation of China under Grant Nos. 61503404 and 42176195.

ORCID iDs

Qiushuo Wei https://orcid.org/0000-0001-6536-7151
Feng Zha https://orcid.org/0000-0002-1864-6876
Lubin Chang https://orcid.org/0000-0002-6705-3401

References

[1] Titterton D H and Weston J L 2004 Strapdown inertial navigation technology *Aerospace & Electronic Systems Magazine. IEEE* (https://doi.org/10.1049/PBRA017E)
[2] Tazartes D 2014 An historical perspective on inertial navigation systems *2014 Int. Symp. on Inertial Sensors and Systems (ISISS)* (*Laguna Beach, CA, USA*, 25–26 *February 2014*) pp 1–5
[3] Qin Y-Y 2006 *Inertial Navigation* (Beijing: Science Press)
[4] Draper C 1981 Control, navigation and guidance *IEEE Control Syst. Mag.* **1** 4–17
[5] Li K and Gao P Y 2019 Research on self-calibration technique for hybrid inertial navigation system *Chin. J. Sci. Instrum.* **40** 9–17
[6] Li J, Guo S, Cui G and Chen C 2018 Polar underwater calibration for strapdown inertial navigation system *Chin. J. Sci. Instrum.* **39** 51–58
[7] Yu X-D 2011 *Research on some key technologies for single-axis rotation inertial navigation system with mechanically dithered ring laser gyroscope* (Changsha: National University of Defense Technology) (https://doi.org/10.7666/d.d159996)
[8] Wei G 2013 *Research on some key technologies for dual-axis rotation inertial navigation system with mechanically dithered ring laser gyroscope* (Changsha: National University of Defense Technology)
[9] Yuan B, Liao D and Han S 2012 Error compensation of an optical gyro INS by multi-axis rotation *Meas. Sci. Technol.* **23** 91–95
[10] Yuan B and Rao G 2006 On the theory of optical gyro rotating inertial navigation system *Natl Univ. Def. Technol.* **28** 76–80
[11] Xie Y-P *et al* 2021 Optimal design of rotation scheme of dual-axis rotation modulation SINS *J. Chin. Inertial Technol.* **29** 421–427+436
[12] Yang Y and Miao L-J 2004 Fiber-optic strapdown inertial system with sensing cluster continuous rotation *IEEE Trans. Aerosp. Electron. Syst.* **40** 1173–8
[13] Levinson E and Majure R 1987 Accuracy enhancement techniques applied to the marine ring laser inertial navigator (MARLIN) *Navigation* **34** 64–86
[14] Zha F, Chang L and He H 2020 Comprehensive error compensation for dual-axis rotational inertial navigation system *IEEE Sens. J.* **20** 3788–802
[15] Syed Z and Aggarwal P 2007 A new multi-position calibration method for MEMS inertial navigation systems *Meas. Sci. Technol.* **18** 1897–907
[16] Gao W, Zhang Y and Wang J 2015 Research on initial alignment and self-calibration of rotary strapdown inertial navigation systems *Sensors* **15** 3154–71
[17] Lahham J I 1992 Acoustic noise reduction in the MK 49 Ship's inertial navigation system (SINS) *IEEE Position Location and Navigation Symp.* (*Monterey, CA*) pp 32–39
[18] Levinson E 1994 The next generation marine inertial navigator is here now *IEEE Position Location and Navigation Symp.* pp 121–7
[19] Levinson E 1980 Laser gyro potential for long endurance marine navigation *IEEE Position Location Navigation Symp.* (*Atlantic City, NJ*) pp 115–29
[20] Heckman D W and Baretela L M 2000 Improved affordability of high precision submarine inertial navigation by insertion of rapidly developing fiber optic gyro technology *IEEE Position Location and Navigation Symp.* (*San Diego, CA*) pp 404–10
[21] Sun F, Sun W and Guo Z 2009 Auto-compensation method of SINS based on IMU rotation *Chin. J. Sci. Instrum.* **2009** 53–59
[22] Zhou Z, Wang X and Cai Y 2020 Design scheme of optimal rotation order for dual-axis rotation modulation *Aero Weaponry* **27** 81–88
[23] Xu Z H *et al* 2020 Carrier kinematics aided two-axis rotary modulation inertial navigation algorithm *Syst. Eng. Electron.* **42** 2066–70
[24] Ji Z-N, Liu C, Cai S-J, Xu H G and Zhou Z H 2013 Improved sixteen-sequence rotation scheme for dual-axis SINS *J. Chin. Inertial Technol.* **21** 46–50